Universal interface engineering method for applying transition metal oxides in silicon heterojunction solar cell

Cao, Liqi; Procel, Paul; Zhao, Yifeng; Yan, Jin; Özkol, Engin; Kovačević, Katarina; Zeman, Miro; Mazzarella, Luana; Isabella, Olindo

DOI
10.1016/j.solmat.2024.113170

Publication date
2024

Document Version
Final published version

Published in
Solar Energy Materials and Solar Cells

Solar Energy Materials & Solar Cells 278 (2024) 113170

Contents lists available at ScienceDirect

Solar Energy Materials and Solar Cells

journal homepage: www.elsevier.com/locate/solmat

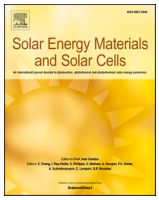

Universal interface engineering method for applying transition metal oxides in silicon heterojunction solar cell

Liqi Cao *, Paul Procel, Yifeng Zhao, Jin Yan, Engin Özkol, Katarina Kovačević, Miro Zeman, Luana Mazzarella, Olindo Isabella

Photovoltaic Materials and Devices Group, Delft University of Technology, Delft, the Netherlands

ARTICLE INFO

Keywords:
Transition metal oxides
Silicon heterojunction solar cells
Industrial approach
Interface engineering

ABSTRACT

Transition metal oxide (TMO) thin films exhibit large bandgap and hold great potential for enhancing the performance of silicon heterojunction (SHJ) solar cells by increasing the short-circuit current density significantly. On the other hand, achieving precise control over the electrical properties of TMO layers is crucial for optimizing their function as efficient carrier-selective layer. This study demonstrates a general and feasible approach for manipulating the quality of several TMO films, aimed at enhancing their applicability in silicon heterojunction (SHJ) solar cells. The core of our method involves precise engineering of the interface between the TMO film and the underlying hydrogenated intrinsic amorphous silicon passivation layer by managing the reaction of the TMO on the surface. X-ray photoelectron spectroscopy spectra demonstrate that our methods can modify the oxygen content in TMO films, thereby adjusting their electronic properties. By applying this method, we have successfully fabricated WO_x-based SHJ solar cells with 23.30 % conversion efficiency and V_2O_x-based SHJ solar cells with 22.04 % conversion efficiency, while keeping *n*-type silicon-based electron-transport layer at the rear side. This research paves the way for extending such interface engineering methods to other TMO materials used as hole-transport layers in SHJ solar cells.

1. Introduction

The photovoltaic industry is predominantly powered by crystalline silicon-based solar cells, with silicon heterojunction (SHJ) solar cells achieving world-record conversion efficiency [1]. In the quest for even higher efficiency and more cost-effective production, researchers are exploring novel materials whose optical and electrical properties are comparable or superior to the traditional boron- and phosphorus-doped silicon-based thin films [2]. Such materials, also known as *dopant-free materials*, include organic films [3,4], metal alkalis [5–7] and transition metal oxides (TMOs) [8–15]. The dopant-free concept is to state that there is no intentional doping in the materials. Dopant-free materials have been successfully integrated into silicon solar cells and have shown promising results. The primary benefit of using dopant-free materials is their low parasitic absorptance which ascribe to their wide band gap [16]. Additionally, their deposition rate is faster than that of *p*-type Si layers [17] and SHJ solar cells can work efficiently with ultrathin TMO materials, unlike *p*-type Si layers that require much thicker films [8]. In recent developments, silicon solar cells featuring dopant-free materials as carrier-selective layer have achieved efficiencies beyond 23 % [18–20]. Meanwhile mainstream front/back-contacted (FBC) SHJ solar cells are based on the rear junction (RJ) structure, implying the deployment of the electron-transport layer (ETL) on the front side [21,22] and *n*-type bulk c-Si wafer. However, to exploit the optical advantage of TMO materials, a TMO-based hole-transport layer (HTL) is used at the front side of (monofacial) SHJ solar cells, known as the front junction (FJ) structure. We obtain a notable achievement in J_{SC} (40.2 mA/cm^2), resulting in a 23.83 % efficiency by integrating an ultra-thin MoO_x as HTL in FJ-SHJ solar cells [8]. Further, substituting traditional Si-based carrier-transport layers with MoO_x for holes and LiF for electrons yielded 21.4 % efficiency in FBC architecture [23], which was further increased to 23.61 % when integrated into an interdigitated back contact (IBC) architecture [24]. Recently, 22.8 % efficiency has been achieved for an FBC RJ-SHJ cell featuring MgO_x/ZnO:Al and V_2O_x as ETL and HTL, respectively [20].

However, the significant potential for improving further cell performance remains unexplored. Simulation results indicate that under optimized conditions, a SHJ solar cell featuring doped silicon-based thin

* Corresponding author.
E-mail address: l.cao-3@tudelft.nl (L. Cao).

https://doi.org/10.1016/j.solmat.2024.113170
Received 25 June 2024; Received in revised form 9 September 2024; Accepted 9 September 2024
Available online 24 September 2024

films as charge-transport layers can achieve a conversion efficiency well above 27 % [25]. Also using TMOs as charge-transport layers could increase this efficiency to 26.96 % [26] or even more than 27 % considering the deployment of high resistivity wafers [25]. This advantage is primarily attributed to the wider bandgap of TMO materials, which facilitates an increased J_{SC}. Nonetheless, in experimental scenarios, the peak efficiency achieved is still limited to 23.83 % [8]. The thermolytic instability of TMOs presents a significant limitation [27,28]. Although some tested materials, such as TiN_x, exhibit chemical stability [29], most dopant-free materials tend to be unstable and are adversely affected by neighboring materials [30,31]. Particularly, in SHJ solar cells, the critical issue involves the reaction between the TMO and the Si-based layers underneath, forming a thin SiO_x film [32–35]. This interaction results into (i) an additional dielectric barrier for charges to cross and (ii) an uncontrolled decrease of the TMO work function, consequently impairing the electronic performance of the device [27,36,37].

Some groups reported on approaches to alleviate the interface reaction of TMOs which results in higher conversion efficiency. For instance, the use of a pre-annealing step can be applied to reduce the hydrogen content from the intrinsic passivation layer, alleviating the reaction between MoO_x and the passivation layer [38]. Notably, inserting a less reactive layer is another solution. Li et al. show that the efficiency can be improved by inserting a CrO_x buffer layer to protect MoO_x [39]. Tong et al. apply a pre-growth SiO_x thin film to prevent the reaction between MoO_x and the substrate [36]. Multilayer structure including $Al_yTiO_x/Ti_yZnO_x/TiO_x/ZnO$ builds up resilience against moisture and therefore improves the stability of TiO_x-based electron-selective contact [40]. Other works apply thicker TMO (V_2O_x and WO_x) films to realize an appropriate high work function, but as a downside effect the resistivity of the TMO films increased significantly resulting in poorer electronic performance of the device [41–43]. Finally, in our previous work we proposed a plasma treatment with or without boron (PTB or PT) before the deposition of MoO_x [8,44,45]. These treatments have been proven to not be harsh against (*i*)a-Si:H [45]. The boron atoms may act as a catalyst to form a favourable interface layer improving the electronic property of devices. These methods improve the efficiency significantly in both monofacial [8,45] and bifacial SHJ solar cells [46].

This contribution aims at showing the applicability of our plasma treatment method to other TMO materials, namely WO_x and V_2O_x, to act as HTLs in SHJ solar cells. Initially, we measure the oxygen content of the TMO films under different interface engineering methods (noPT, PT and PTB). Subsequently, we study the impact of those methods on the performance of SHJ solar cells as function of WO_x and V_2O_x thicknesses. We ultimately showcase high-efficiency FJ-SHJ solar cells (23.30 % and 22.04 %) integrating 2-nm thick WO_x and 3-nm thick V_2O_x films, respectively, and n-type Si-based ETL.

2. Experimental methods

Fig. 1 presents the structure of TMO-based FJ-SHJ solar cells. These samples were fabricated using <100> n-type, double-sided polished, 4-inch float-zone (FZ) wafers. The wafers exhibited a thickness of 280 ± 20 μm and a resistivity of 3 ± 2 Ω cm. For texturing, the wafers were processed in a tetramethylammonium hydroxide (TMAH) solution, with ALKA-TEX serving as an additive. The cleaning process entailed a wet chemical treatment, followed by immersion in a 0.55 % hydrogen fluoride (HF) solution for 5 min. Subsequently, the wafers were placed into a plasma-enhanced chemical vapor deposition (PECVD) system for the deposition of thin-film layers. The (*i*)/(*n*)a-Si:H stack at the rear side was kept constant across all solar cells involved in this study [47,48]. We are using 7-nm thick and 5-nm thick (*i*)a-Si:H on the front and rear side, respectively. The (*n*)a-Si:H on the rear side is 4-nm thick. Subsequently, the deposition of the (*i*)a-Si:H and the application of different plasma treatment methods were performed on the front side. These methods are

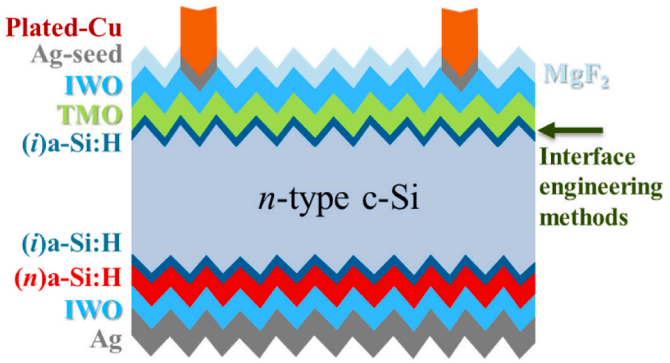

Fig. 1. Cross-sectional sketch of a TMO-based FJ-SHJ solar cell.

processed in the PECVD chamber. Three methods are tested namely, noPT (no treatment), PT (plasma treatment) and PTB (plasma treatment with boron), which use a gas mixture including SiH_4, H_2, CO_2, and B_2H_6, as provided in Table S1. For detailed information on the interface engineering process, readers are referred to our previous work [8,45]. Then, TMO thin films (WO_x and V_2O_x) were thermally evaporated under a vacuum pressure of $5x10^{-6}$ mbar with thicknesses of 1, 2, 3, 4, and 5 nm. The deposition rate of both TMOs is 0.1 nm/s. The substrate rotated at the speed of 10 rpm. For comparative analysis, a reference FJ-SHJ solar cell featuring a *p*-type Si layer at the front side is also included; more experimental details about that can be found elsewhere [49]. Following the TMO deposition, layers of optimized tungsten-doped indium oxide (IWO) were sputtered onto both the front and rear sides, with thicknesses of 50 nm and 150 nm, respectively [50]. A hard mask was employed to define six 2 × 2 cm^2 solar cells on each wafer during the IWO deposition process. The samples were annealed at 180 °C for 5 min to recover from the sputtering damage. Following this step, a 100-nm thick layer of silver was sputtered onto the front side, which was then followed by copper plating to establish the metallic contact grid [51,52]. The fingers were 15-μm wide with a pitch of 915 μm. 500 nm of silver was sputtered as the rear metal electrode. Subsequently, the front side was coated with a 110-nm thick layer of MgF_2, serving - together with the front IWO - as a double antireflection coating. The specified thicknesses were derived using a nominal calculation, modified by a geometrical factor of 1.7 to consider the lower deposition rate on textured surface [53].

The effective minority carrier lifetime was measured after each step of the fabrication process using a Sinton WCT-120. To evaluate the current-voltage (*J-V*) performance under standard test conditions an AAA rated Wacom WXS-90S-L2 solar simulator was utilized. Additionally, in-house external quantum efficiency (EQE) equipment was used to measure $J_{SC,EQE}$. The absorptance spectra were measured on TMO layers deposited on Corning glass using a PerkinElmer Lambda 1050 system. The sketch of the samples for absorbance measurement is shown in Fig. S1. Spectral response analyses were conducted on dedicated cells on the same wafer as other solar cells but without the front metal grid. For the compositional analysis of the TMO layers, we employed a Thermo-Fisher *K*α X-ray photoelectron spectrometer (XPS) [54,55], utilizing an Al *K*α X-ray source (1486.68 eV) within a chamber maintaining a base pressure of 2 × 10^{-9} mbar. These measurements were executed at room temperature following the attainment of a high vacuum. Notably, the XPS sample prepared with identical processes depicted in Fig. S2, using 280 ± 20 μm flat <111> *n*-type float-zone (FZ) wafers to replicate the surface orientation of the pyramid facets observed in solar cells, with deposition times adjusted to align the thicknesses with those of textured samples.

3. Result and discussion

3.1. Control the oxygen content of WO_x and V_2O_x

TMOs exhibit similar properties, particularly where oxygen content influences their work function [31]. Drawing from observations in prior research [8,27,45,56–59], we speculate that the influence observed in other TMO materials, such as MoO_x, would similarly affect WO_x and V_2O_x. To demonstrate our speculation, we conduct XPS analyses to explore the oxygen vacancies in these films. The high-resolution spectra and the full XPS survey spectra of W and V are reported in Figs. S3 and S4, respectively. Additionally, the boron atoms have not been detected through XPS high resolution scan as shown in Fig. S5. For our experiments, we use films with thicknesses of 2 nm for WO_x and 3 nm for V_2O_x. These thickness values were chosen based on our previous study, where we achieved a champion device with 2 nm MoO_x [8]. The corresponding valence band spectra are plotted in Fig. 2. The shoulder peaks noticeable between 1 eV and 2 eV in the valence band spectra of WO_x and V_2O_x indicate the presence of defects in the films. The observed defects stem from the TMOs' instability, leading to interface reactions between (*i*) a-Si:H and the TMOs, which result in the formation of a thin SiO_x film [8]. This process extracts oxygen from TMO molecules, creating oxygen vacancies in the material and thereby changing their work function [45].

Valence band spectra as provided in Fig. 2 reveal that V_2O_x-films exhibit higher peak heights compared to WO_x, suggesting that V_2O_x contains a larger number of defects, i.e. oxygen vacancies. This phenomenon can be attributed to the fact that the binding energy of the W-O bond (>5.0 eV) [60] exceeds that of the V-O bond (~4.3 eV) [61]. Consequently, the V-O bond is weaker resulting in easier oxygen reactions with the substrate. Defects within TMO films present a dual-edged sword. On the one hand, these defects significantly impact the electronic properties of the device. On the other hand, these vacancies endow the films with semiconductor properties, specifically facilitating carrier-selective layer [62,63]. Nonetheless, an overabundance of oxygen vacancies may impair carrier transport efficiency [59]. Therefore, it is crucial to identify a TMO material that establishes a balance between the quantity of oxygen vacancies and its capacity for selective transport.

To elaborate further, within each category of TMOs, the distinctions in oxygen vacancies may initially appear subtle as shown in Fig. 2.

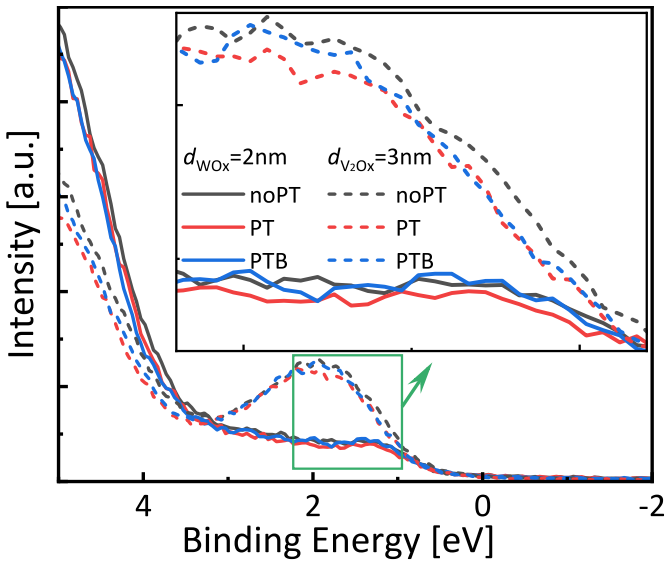

Fig. 2. Valence band spectra of as-deposited 2-nm thick WO_x and 3-nm thick V_2O_x films deposited after noPT, PTB and PT methods. The inset shows a zoomed view of the spectra between 1 eV and 2 eV binding energy.

However, upon closer examination at an enlarged scale in Fig. 2, it becomes evident that the PT method results in fewer oxygen vacancies within the films followed by PTB and noPT cases. To substantiate these observations, we report the oxygen content within these films extracted from the XPS survey spectra. The tungsten, vanadium and oxygen content of the films expressed in percentage are presented in Fig. 3A and B, offering quantitative insights into the variations of oxygen content across different methods. We observe that interface engineering methods significantly affect the oxygen ratio within the films. Specifically, for both WO_x and V_2O_x films, the PT samples exhibit the highest oxygen concentrations. The presence of increased oxygen concentrations in the films correlates with fewer oxygen vacancies, aligning with the insights obtained from the valence band spectra analysis discussed above in Fig. 2.

3.2. Performance of WO_x-based SHJ solar cells

The efficiency of carriers transport within TMO materials is critically dependent on their work function [64], which is influenced by the internal oxygen content [27]. Moreover, the thickness of the film plays a crucial role in determining this oxygen content [8,65,66]. To understand these dynamics, we have examined the effects of film thickness and interface engineering methods on solar cell performance. Fig. 4 shows the external parameters derived from the *J-V* curve of solar cells with variable WO_x thicknesses and noPT, PT and PTB methods.

For the devices with noPT as shown in Fig. 4A–D, we observe that V_{OC} drops with thicker WO_x films. It is important to mention that the 2-nm samples exhibited a significant decline in performance, which can be attributed to the reduced minority carrier lifetime (τ) of the cell precursor as shown in Fig. S6. The τ measured after the deposition of WO_x dropped more than half of the τ measured after the PECVD process. The drop may be attributed to the reaction between WO_x and the passivation layer deposited by PECVD. The higher V_{OC} measured for the 1-nm thick WO_x might be explained by the higher initial passivation quality (higher τ, see Fig. S6) for this specific precursor. For the fill factor (*FF*) we observe a linear increase from 65 % up to 78 % for a WO_x thickness from 1 to 4 nm. For 5-nm thick WO_x the *FF* drops to 70 %. This trend suggests a critical balance between WO_x-thickness and *FF*, identifying 4 nm as the optimal thickness. The J_{SC} decreases as the WO_x thickness increases. The absorbance data, shown in Fig. S7, indicate that WO_x layers absorb short-wavelength light more effectively, with increased absorptance in thicker layers. For the 5-nm thick sample, the rise in J_{SC} might be attributed to optimal combination of antireflection coating. The conversion efficiency (η) is mostly dominated by the *FF* trend with the highest η of 21.29 % measured for 4-nm thick WO_x film.

For the solar cells fabricated with PT method, we observe an opposite trend with respect to the V_{OC} as provided in Fig. 4E. V_{OC} increases with thicker WO_x films and arrives at the optimal point at 4 nm with a subsequent decline for 5-nm thick WO_x. During the PT process, thin layers of (*i*)nc-Si:H and (*i*)nc-SiO_x:H are deposited under rather aggressive PECVD conditions, which may degrade passivation quality [8,49]. Consequently, V_{OC} is lower in the case of 1-nm thick WO_x for PT compared to noPT. With increasing WO_x thickness, there is an enhancement in the work function of WO_x, which contributes to better carrier selectivity at the interface between c-Si and (*i*)a-Si:H [8,67]. However, the decrease in V_{OC} for samples featuring WO_x thicker than 4 nm can be ascribed to a dipole formation at (*i*)a-Si:H/WO_x, which penalizes V_{OC} and *FF*, similarly to what was observed on samples using MoOx [8]. Indeed, V_{OC} and *FF* exhibit similar trends as depicted in Fig. 4E and F, peaking for an optimal 4-nm thick WO_x layer. This trend, observed also for the noPT case, indicates that the film's work function gets higher for thicker WO_x layers. However, further thickening the WO_x layer to 5 nm caused a decrease in *FF*, highlighting the need to balance the work function and the contact resistivity [8,18]. Similarly to what was observed for noPT, in Fig. 4G, the J_{SC} decreases with the increase of WO_x thickness. For the 5-nm thick sample, the observed rise in J_{SC} could

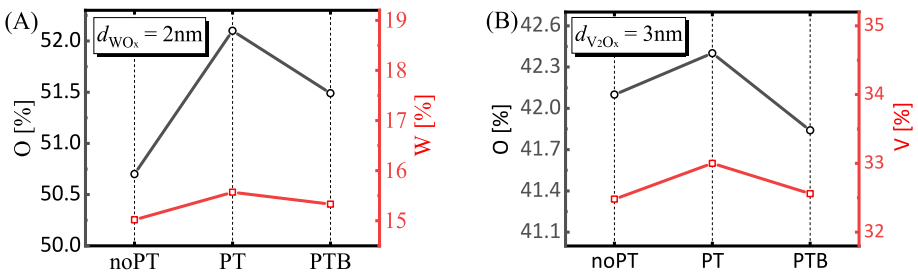

Fig. 3. (A) W and O content, (B) V and O content under different interface engineering methods calculated from XPS spectra (see Figs. S3 and S4).

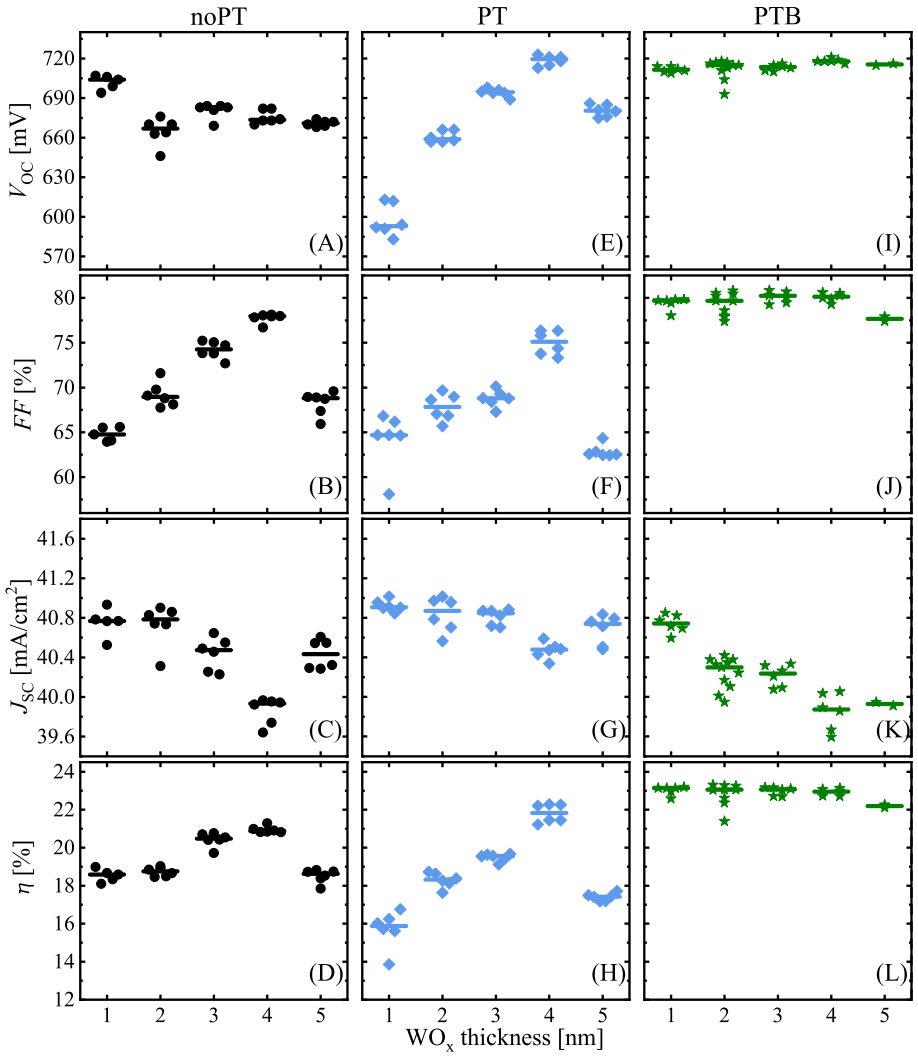

Fig. 4. The parameters extracted from *J-V* curve of solar cells with different interface engineering methods and WO_x thickness. (A–D) represent the noPT method with black circles; (E–H) represent the PT method with blue diamonds; (I–L) represent the PTB method with green stars. The short lines indicate average values.

be attributed to the optimal combination of antireflection coatings. The η trend aligns with those of V_{OC} and *FF*, with the highest conversion η of 22.27 % realized for a 4-nm thick WO_x layer.

Finally, we discuss the impact of PTB, shown in Fig. 4I–L. V_{OC} remains generally stable but is slightly higher at a thickness of 2 nm. From lowest to higher thickness value, the *FF* slightly increases, reaches the highest value at 3 nm, and decreases with further increased thickness of WO_x. The champion *FF* is over 80 %. Compared to noPT and PT cases, the *FF* is improved significantly and shows less dependence on the thickness of WO_x. Similarly to the previous cases, J_{SC} decreases for thicker layers. The optimal η of 23.30 % is observed at 2 nm. The trend of η suggests that the working windows of the thickness of WO_x with PTB is wider than the other two methods.

We can conclude that, across different conditions, V_{OC} performance differs depending on the interface engineering method used. The *FF* generally rises for thicker layers before decreasing for the thicker film tested demonstrating a trade-off between work function and contact resistivity. Interestingly the variations of V_{OC} and *FF* are much less impacted by the WO_x thickness for the samples with PTB. This could be due to the interface becoming less reactive with WO_x after being modified by the PTB method. Generally, J_{SC} decreased as the WO_x film thickness increased because of parasitic absorptance. Still, η follows the

trend of *FF*. With PTB and 2-nm thick WO_x, we achieve a champion cell with a conversion efficiency of 23.30 %. Similarly to our previous work [8], it is worth noting that no boron atom is detected through XPS measurement for PTB samples. The thinner optimal thickness of WO_x with PTB comes from the optimal interface engineering and achieves a good balance between work function and defects of the WO_x film. We also present the external quantum efficiency (EQE) and *J-V* curves of the champion WO_x-based and MoO_x-based FJ-SHJ devices [8] in Fig. 5. Additionally, Fig. 5 showcases the champion RJ-SHJ solar cell with doped layers from our lab [68]. Remarkably, there is a gain in $J_{SC,\ EQE}$ (indicated by the green area in Fig. 5A) at short wavelengths when using TMOs, attributed to reduced parasitic absorptance on the front side as compared to SHJ solar cells with doped layers.

3.3. Performance of V_2O_x-based SHJ solar cells

We now examine the impact of V_2O_x-thickness and interface engineering methods on the performance of solar cells, whose parameters, extracted from *J-V* measurements, are plotted in Fig. 6.

As provided in Fig. 6A–D, a gradual decrease in V_{OC} with V_2O_x thickness is observed in noPT condition. As previously discussed, TMOs will react with the substrate which is (*i*)a-Si:H in this case, forming a SiO_x layer. This reaction degrades the passivation quality provided by the (*i*)a-Si:H layer. As we observed in WO_x samples with noPT method, we suppose the reaction is related to the thickness of V_2O_x as well. The thicker layer may cause a more significant reaction resulting in lower V_{OC}. The higher V_{OC} at 4 nm case could be attributed to the high lifetime of the precursor as shown in Fig. S8. J_{SC} shows a decline with increased V_2O_x thickness. Fig. S9 provides the absorptance spectra for different thicknesses of V_2O_x. The absorptance of V_2O_x films increases as the film thickness increases. The increase of J_{SC} at 5 nm for noPT samples might be caused by the optimized combination of antireflection coating. The *FF* decreases with V_2O_x thickness, which could be due to increased sheet resistance as the V_2O_x layer gets thicker. η increased slightly and peaked at 4 nm before decreasing at 5 nm.

Like PT-treated WO_x-based SHJ devices, the V_{OC} of V_2O_x samples in Fig. 6E shows a slight increase with V_2O_x thickness, except for the 2-nm case, peaking at 4 nm and then decreasing at 5 nm. The decrease at 5 nm may be ascribed to thicker V_2O_x film blocking the carrier transport. In Fig. 6F, *FF* shows a peak at 4 nm. This phenomenon can be attributed to the same reasoning as in the WO_x case, representing the balance between carrier selectivity and contact resistivity [8,18]. Additionally, the increase in layer thickness leads to a decrease in J_{SC} due to parasitic absorptance as shown in Fig. 6G. PT samples show η peak at 4 nm thickness, pointing to an optimal thickness for device performance.

The data of devices manufactured with the PTB method are presented in Fig. 6I–L. V_{OC} shows a slight increase with increasing V_2O_x thickness. The interlayer deposited during PTB maintains a good balance between passivation degradation caused by interface reaction and the passivation effect introduced by V_2O_x. J_{SC} decreases with thicker layers. PTB samples achieve their peak *FF* at 3 nm, demonstrating improved control of interface reactions and the electronic properties of the V_2O_x layer. η follows a similar trend to *FF*. The champion cell with η of 22.04 %, was obtained for a V_2O_x thickness of 3 nm.

The general trends observed in the parameters of V_2O_x-based cells resemble those of WO_x-based cells, as discussed in Section 3.2. This similarity suggests that the applied methods to different TMOs yield comparable results. At the device level, *FF* is identified as the predominant factor affecting solar cell performance. PTB samples exhibit the highest *FF* at thinner TMO-thickness compared to PT and noPT methods, leading to the champion devices being achieved using the PTB method for both WO_x and V_2O_x cases. Specifically, the η of V_2O_x-based SHJ solar cells is generally lower than that of WO_x-based cells, primarily due to material properties [55,69]. The weaker V-O bond contributes to more severe interface reactions between V_2O_x and substrate [60,61]. The reaction generates more defects at the interface which harm the carrier transport. This aligns with our findings from the valence band spectra analysis as provided in Fig. 2. Additionally, we provide the EQE of the champion V_2O_x-based SHJ solar cells and the SHJ solar cell with doped layers in Fig. 5. At short wavelengths, a notable $J_{SC,\ EQE}$ gain is observed. This gain (shown by the green shaded area in Fig. 5A) is achieved with V_2O_x, attributed to reduced parasitic absorptance on the front side compared to SHJ solar cells with doped layers.

4. Conclusion

In this work, we utilized different interface engineering methods (noPT, PT and PTB) to alleviate the interface reaction of TMO with the substrate. We investigated the effect of different methods by estimating the TMOs' oxygen content. From XPS survey spectra, we observed that oxygen content in TMO layers deposited after PT is higher than that in TMO layers deposited with PTB and noPT methods. The findings aligned with our previous results and proved the PTB method able to control and create a suitable deposition condition for TMOs, ensuring their suitable work function and oxygen content inside the films. With this observation, further experiments are applied to investigate the impact of TMO-thickness on cell performance regarding different methods.

Overall, we applied different methods (noPT, PT and PTB) at the (*i*)a-

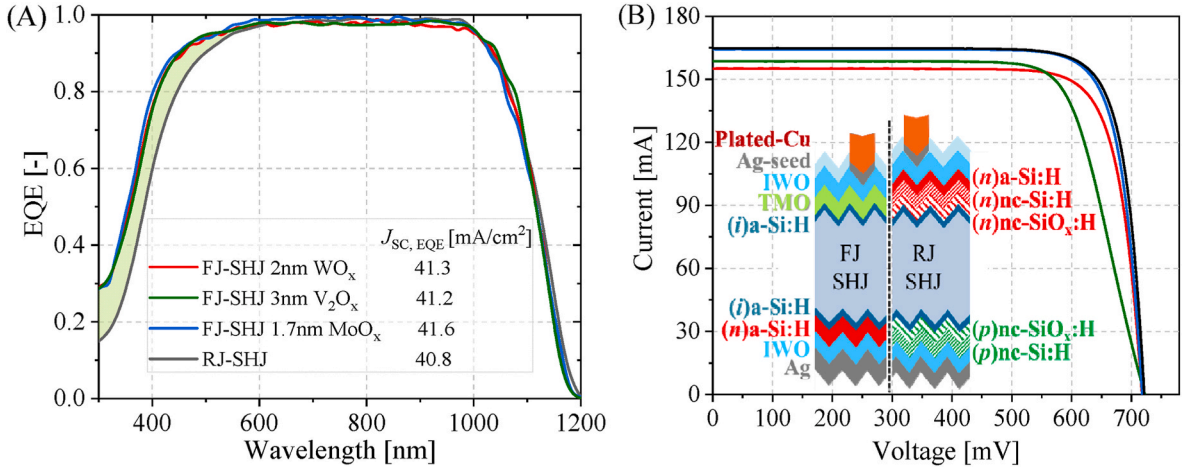

Fig. 5. (A) EQE and (B) *J-V* curves of champion WO_x-based (red), V_2O_x-based (green), MoO_x-based (blue) FJ-SHJ solar cell and RJ-SHJ solar cell with doped layers (black). The green shaded area in (A) represents the photocurrent density gain when switching solar cell structure from RJ-SHJ endowed with silicon transport layers to FJ-SHJ endowed with TMO as HTL. In (B) the detailed layer structure of RJ-SHJ solar cell with doped layers is depicted.

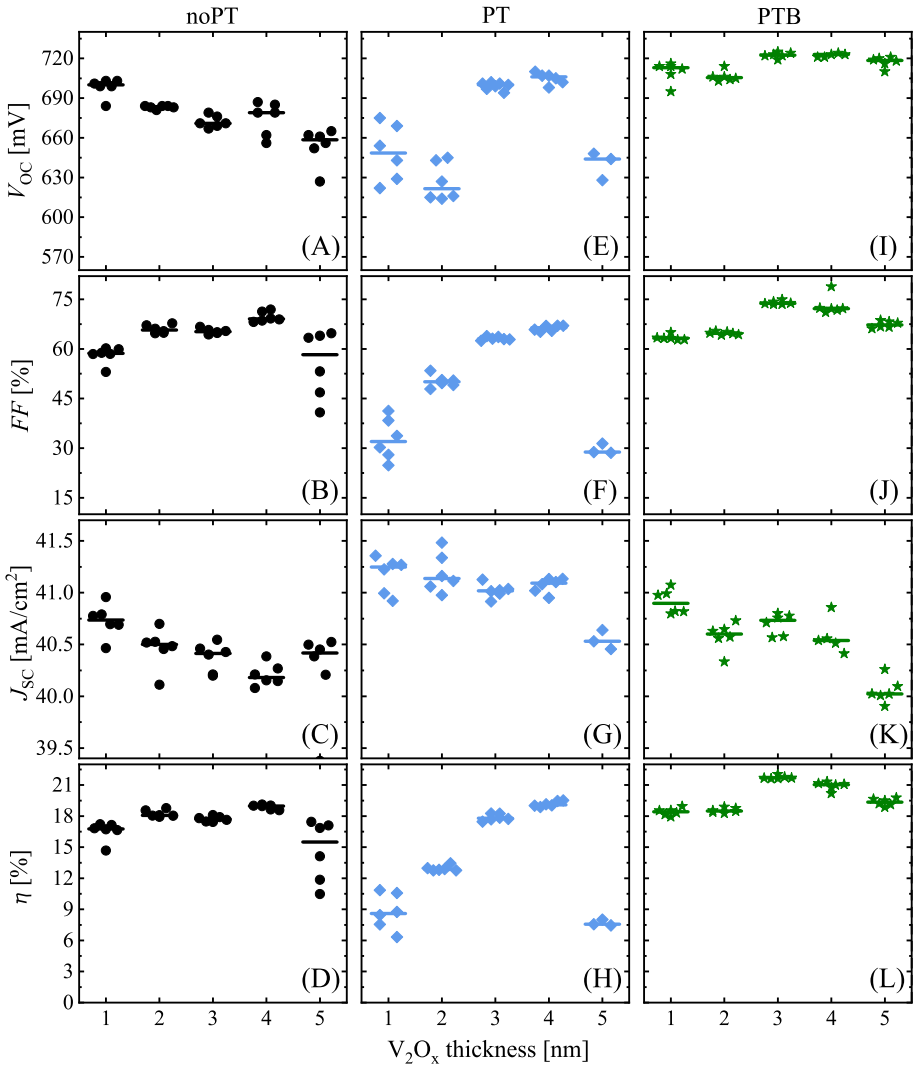

Fig. 6. The parameters extracted from *J-V* curve of solar cells with different interface engineering methods and V_2O_x thickness. (A–D) represent the noPT method with black circles; (E–H) represent the PT method with blue diamonds; (I–L) represent the PTB method with green stars. The short lines indicate average values.

Si:H/WO_x interface and realized a champion cell with PTB and 2-nm thick WO_x HTL. With 23.30 % conversion efficiency and *FF* equal to 80.80 %, we push further the performance of WO_x-based SHJ solar cells. Similarly, we modified the (*i*)a-Si:H/V_2O_x interface with the same methods and realized a champion cell with PTB and 3-nm thick V_2O_x HTL, exhibiting 22.04 % conversion efficiency and *FF* equal to 74.88 %. Our TMO-based FJ-SHJ solar cells' results reveal that the PTB is a method that creates an optimal surface condition for the deposition of TMOs and achieves a desirable equilibrium between the quantity of defects and carrier transport of the film, leading to the enhanced performance of TMO-based SHJ solar cells. We may conclude that PTB has the potential to be extended to other TMO materials serving as HTLs in SHJ solar cells, suggesting a broader applicability of this method in enhancing device performance. Furthermore, the PTB method is compatible with industrial SHJ production lines.

CRediT authorship contribution statement

Liqi Cao: Writing – review & editing, Writing – original draft, Visualization, Validation, Methodology, Investigation, Formal analysis, Data curation, Conceptualization. **Paul Procel:** Writing – review & editing, Methodology. **Yifeng Zhao:** Writing – review & editing, Validation, Methodology. **Jin Yan:** Formal analysis. **Engin Özkol:** Writing – review & editing. **Katarina Kovačević:** Writing – review & editing. **Miro Zeman:** Writing – review & editing, Funding acquisition. **Luana Mazzarella:** Writing – review & editing, Supervision, Methodology, Conceptualization. **Olindo Isabella:** Writing – review & editing, Validation, Supervision, Project administration, Methodology, Funding acquisition, Conceptualization.

Declaration of competing interest

The authors declare the following financial interests/personal relationships which may be considered as potential competing interests:

Liqi Cao reports financial support was provided by China Scholarship Council. If there are other authors, they declare that they have no known competing financial interests or personal relationships that could have appeared to influence the work reported in this paper.

Data availability

Data will be made available on request.

Acknowledgment

The authors thank Martijn Tijssen, Stefaan Heirman, Bernardus Zijlstra, Tim Velzeboer, Shuang Hao and Bart Boshuizen for their technical support. Liqi Cao would like to thank China Scholarship Council

(CSC NO. 202006740021) for the financial support.

Appendix A. Supplementary data

Supplementary data to this article can be found online at https://doi.org/10.1016/j.solmat.2024.113170.

References

[1] H. Lin, et al., Silicon heterojunction solar cells with up to 26.81% efficiency achieved by electrically optimized nanocrystalline-silicon hole contact layers, Nat. Energy 8 (8) (2023) 789–799, https://doi.org/10.1038/s41560-023-01255-2.

[2] J. Bullock, et al., Efficient silicon solar cells with dopant-free asymmetric heterocontacts, Nat. Energy 1 (3) (2016), https://doi.org/10.1038/NENERGY.2015.31.

[3] J. Yan, et al., Stable organic passivated carbon nanotube–silicon solar cells with an efficiency of 22, Adv. Sci. 8 (20) (2021), https://doi.org/10.1002/advs.202102027.

[4] L.P. Yu, A.S.R. Bati, T.S.L. Grace, M. Batmunkh, J.G. Shapter, Ti3C2Tx (MXene)-Silicon heterojunction for efficient photovoltaic cells, Adv. Energy Mater. 9 (31) (2019), https://doi.org/10.1002/aenm.201901063.

[5] W. Wang, et al., Cerous fluoride dopant-free electron-selective contact for crystalline silicon solar cells, Phys. Status Solidi Rapid Res. Lett. 15 (12) (2021), https://doi.org/10.1002/pssr.202100135.

[6] C. Xing, et al., Post-annealing-free BaOxFy/LiF-based stack electron-selective contacts for high efficiency crystalline silicon solar cells featuring ultra-low contact resistivity, Chem. Eng. J. 481 (2024) 148568, https://doi.org/10.1016/j.cej.2024.148568.

[7] J. Li, et al., One-step formation of low work-function, transparent and conductive MgFxOy electron extraction for silicon solar cells, Adv. Sci. 9 (23) (2022), https://doi.org/10.1002/advs.202202400.

[8] L. Cao, et al., Achieving 23.83% conversion efficiency in silicon heterojunction solar cell with ultra-thin MoOx hole collector layer via tailoring (i)a-Si:H/MoOx interface, Prog. Photovoltaics Res. Appl. (2022), https://doi.org/10.1002/pip.3638.

[9] M. Bivour, F. Zähringer, P. Ndione, M. Hermle, Sputter-deposited WOx and MoOx for hole selective contacts, in: Energy Procedia, Elsevier Ltd, 2017, pp. 400–405, https://doi.org/10.1016/j.egypro.2017.09.259.

[10] M. Abdelhameed, M.F. Abdelbar, M. Esmat, W. Jevasuwan, N. Fukata, Hole-injection role of solution-processed thermally treated VOx thin films in Si nanowire-based solar cells, Nano Energy 99 (Aug) (2022), https://doi.org/10.1016/j.nanoen.2022.107373.

[11] Z. Xu, et al., Solution-processed copper-doped chromium oxide with tunable oxygen vacancy for crystalline silicon solar cells hole-selective contacts, Sol. RRL 5 (5) (2021), https://doi.org/10.1002/solr.202100064.

[12] B. Macco, et al., Effective passivation of silicon surfaces by ultrathin atomic-layer deposited niobium oxide, Appl. Phys. Lett. 112 (24) (2018), https://doi.org/10.1063/1.5029346.

[13] M. Nayak, K. Bergum, G.E. Stan, I.H. Lee, A. Kuznetsov, Sub-stochiometric nickel oxide hole-selective contacts in solar cells: comparison of simulations and experiments with sputtered films, Physica Status Solidi (A) Applications and Materials Science 220 (10) (2023), https://doi.org/10.1002/pssa.202200651.

[14] L. Zhang, et al., Low-temperature Ta-doped TiOx electron-selective contacts for high-performance silicon solar cells, Sol. Energy Mater. Sol. Cell. 266 (Mar) (2024), https://doi.org/10.1016/j.solmat.2024.112703.

[15] X. Yang, et al., Atomic layer deposition of vanadium oxide as hole-selective contact for crystalline silicon solar cells, Adv Electron Mater 6 (8) (2020), https://doi.org/10.1002/aelm.202000467.

[16] L. Neusel, M. Bivour, M. Hermle, Selectivity issues of MoOx based hole contacts, in: Energy Procedia, Elsevier Ltd, 2017, pp. 425–434, https://doi.org/10.1016/j.egypro.2017.09.268.

[17] H. Fujiwara, M. Kondo, Effects of a-Si:H layer thicknesses on the performance of a-Si:H/c-Si heterojunction solar cells, J. Appl. Phys. 101 (5) (2007), https://doi.org/10.1063/1.2559975.

[18] J. Dréon, et al., 23.5%-efficient silicon heterojunction silicon solar cell using molybdenum oxide as hole-selective contact, Nano Energy 70 (Apr) (2020), https://doi.org/10.1016/j.nanoen.2020.104495.

[19] J. Bullock, et al., Dopant-free partial rear contacts enabling 23% silicon solar cells, Adv. Energy Mater. 9 (9) (2019), https://doi.org/10.1002/aenm.201803367.

[20] D. Xu, et al., High-performance transparent electron-selective contact for crystalline silicon solar cells, Adv. Funct. Mater. (2024), https://doi.org/10.1002/adfm.202407290.

[21] S. De Wolf, A. Descoeudres, Z.C. Holman, C. Ballif, High-efficiency silicon heterojunction solar cells: a review, green 2 (1) (2012) 7–24.

[22] Z. Sun, et al., Toward Efficiency Limits of Crystalline Silicon Solar Cells: Recent Progress in High-Efficiency Silicon Heterojunction Solar Cells, John Wiley and Sons Inc, 2022, https://doi.org/10.1002/aenm.202200015.

[23] S. Zhong, et al., Mitigating plasmonic absorption losses at rear electrodes in high-efficiency silicon solar cells using dopant-free contact stacks, Adv. Funct. Mater. 30 (5) (2020), https://doi.org/10.1002/adfm.201907840.

[24] Z. Liu, et al., Dual functional dopant-free contacts with titanium protecting layer: boosting stability while balancing electron transport and recombination losses, Adv. Sci. 9 (23) (2022), https://doi.org/10.1002/advs.202202240.

[25] P. Procel, Y. Zhao, Oi Isabella, Sol. Energy Mater. Sol. Cell. (2024). "to be submitted.

[26] Y. Zhao, et al., Strategies for realizing high-efficiency silicon heterojunction solar cells, Sol. Energy Mater. Sol. Cell. 258 (2023), https://doi.org/10.1016/j.solmat.2023.112413.

[27] M.T. Greiner, L. Chai, M.G. Helander, W.M. Tang, Z.H. Lu, Transition metal oxide work functions: the influence of cation oxidation state and oxygen vacancies, Adv. Funct. Mater. 22 (21) (2012) 4557–4568, https://doi.org/10.1002/adfm.201200615.

[28] P. Gao, et al., Dopant-Free and Carrier-Selective Heterocontacts for Silicon Solar Cells: Recent Advances and Perspectives, Wiley-VCH Verlag, 2018, https://doi.org/10.1002/advs.201700547.

[29] X. Yang, et al., Dual-function electron-conductive, hole-blocking titanium nitride contacts for efficient silicon solar cells, Joule 3 (5) (2019) 1314–1327, https://doi.org/10.1016/j.joule.2019.03.008.

[30] G.S. Jeong, et al., Stoichiometry and morphology analysis of thermally deposited V2O5−x thin films for Si/V2O5−x heterojunction solar cell applications, Materials 15 (15) (2022), https://doi.org/10.3390/ma15155243.

[31] M.T. Greiner, Z.H. Lu, Thin-film metal oxides in organic semiconductor devices: their electronic structures, work functions and interfaces, NPG Asia Mater. 5 (7) (2013), https://doi.org/10.1038/am.2013.29.

[32] J. Geissbühler, et al., 22.5% efficient silicon heterojunction solar cell with molybdenum oxide hole collector, Appl. Phys. Lett. 107 (8) (2015), https://doi.org/10.1063/1.4928747.

[33] H. Ali, et al., In situ transmission electron microscopy study of molybdenum oxide contacts for silicon solar cells, Physica Status Solidi (A) Applications and Materials Science 216 (7) (2019), https://doi.org/10.1002/pssa.201800998.

[34] J. Cho, et al., Interface analysis and intrinsic thermal stability of MoOx based hole-selective contacts for silicon heterojunction solar cells, Sol. Energy Mater. Sol. Cell. 201 (Oct) (2019), https://doi.org/10.1016/j.solmat.2019.110074.

[35] L.G. Gerling, C. Voz, R. Alcubilla, J. Puigdollers, Origin of passivation in hole-selective transition metal oxides for crystalline silicon heterojunction solar cells, J. Mater. Res. 32 (2) (2017) 260–268, https://doi.org/10.1557/jmr.2016.453.

[36] J. Tong, et al., Impact of pregrown SiOxon the carrier selectivity and thermal stability of molybdenum-oxide-passivated contact for Si solar cells, ACS Appl. Mater. Interfaces 13 (30) (2021) 36426–36435, https://doi.org/10.1021/acsami.1c06765.

[37] M.T. Greiner, L. Chai, M.G. Helander, W.M. Tang, Z.H. Lu, Metal/metal-oxide interfaces: how metal contacts affect the work function and band structure of MoO3, Adv. Funct. Mater. 23 (2) (2013) 215–226, https://doi.org/10.1002/adfm.201200993.

[38] S. Essig, et al., Toward annealing-stable molybdenum-oxide-based hole-selective contacts for silicon photovoltaics, Sol. RRL 2 (4) (2018), https://doi.org/10.1002/solr.201700227.

[39] J. Li, et al., Bilayer MoOX/CrOXPassivating contact targeting highly stable silicon heterojunction solar cells, ACS Appl. Mater. Interfaces 12 (32) (2020) 36778–36786, https://doi.org/10.1021/acsami.0c09877.

[40] M.M. Shehata, T.N. Truong, G. Bartholazzi, D.H. Macdonald, L.E. Black, Addressing the stability challenges of TiOx-based passivating contacts for high-efficiency c-Si solar cells, J Mater Chem A Mater 12 (15) (2023) 8826–8845, https://doi.org/10.1039/d3ta05951k.

[41] H. Nasser, G. Kökbudak, H. Mehmood, R. Turan, Dependence of n-cSi/MoOx heterojunction performance on cSi doping concentration, in: Energy Procedia, Elsevier Ltd, 2017, pp. 418–424, https://doi.org/10.1016/j.egypro.2017.09.267.

[42] C. Battaglia, et al., Hole selective MoOx contact for silicon solar cells, Nano Lett. 14 (2) (2014) 967–971, https://doi.org/10.1021/nl404389u.

[43] H. Nasser, et al., On the application of hole-selective MoOx as full-area rear contact for industrial scale p-type c-Si solar cells, Prog. Photovoltaics Res. Appl. 29 (3) (2021) 281–293, https://doi.org/10.1002/pip.3363.

[44] P.A.P. Moya, L. Mazzarella, O. Isabella, M. Zeman, Methodology for Efficient Hole Transport Layer Using Transition Metal Oxides, 2021.

[45] L. Mazzarella, et al., Strategy to mitigate the dipole interfacial states in (i)a-Si:H/MoOx passivating contacts solar cells, Prog. Photovoltaics Res. Appl. 29 (3) (2021) 391–400, https://doi.org/10.1002/pip.3381.

[46] L. Cao, et al., Indium reduction in bifacial silicon heterojunction solar cells with MoOx hole collector, Advanced Energy and Sustainability Research (2024), https://doi.org/10.1002/aesr.202400105.

[47] Y. Zhao, et al., Ultra-thin electron collectors based on nc-Si:H for high-efficiency silicon heterojunction solar cells, Prog. Photovoltaics Res. Appl. 30 (8) (2022) 809–822, https://doi.org/10.1002/pip.3502.

[48] Y. Zhao, et al., Doped hydrogenated nanocrystalline silicon oxide layers for high-efficiency c-Si heterojunction solar cells, Prog. Photovoltaics Res. Appl. 28 (5) (2020) 425–435, https://doi.org/10.1002/pip.3256.

[49] Y. Zhao, et al., Design and optimization of hole collectors based on nc-SiOx:H for high-efficiency silicon heterojunction solar cells, Sol. Energy Mater. Sol. Cell. 219 (Jan) (2021), https://doi.org/10.1016/j.solmat.2020.110779.

[50] C. Han, et al., Room-temperature sputtered tungsten-doped indium oxide for improved current in silicon heterojunction solar cells, Sol. Energy Mater. Sol. Cell. 227 (Aug) (2021), https://doi.org/10.1016/j.solmat.2021.111082.

[51] C. Han, et al., Controllable simultaneous bifacial Cu-plating for high-efficiency crystalline silicon solar cells, Sol. RRL 6 (6) (2022), https://doi.org/10.1002/solr.202100810.

[52] G. Limodio, et al., Copper-plating metallization with alternative seed layers for c-Si solar cells embedding carrier-selective passivating contacts, IEEE J. Photovoltaics 10 (2) (2020) 372–382, https://doi.org/10.1109/JPHOTOV.2019.2957671.

[53] E. Özkol, P. Wagner, F. Ruske, B. Stannowski, L. Korte, Optimization of silicon heterojunction interface passivation on p- and n-type wafers using optical emission spectroscopy, Physica Status Solidi (A) Applications and Materials Science 219 (5) (2022), https://doi.org/10.1002/pssa.202100511.
[54] T. Sun, et al., Investigation of MoOx/n-Si strong inversion layer interfaces via dopant-free heterocontact, Phys. Status Solidi Rapid Res. Lett. 11 (7) (2017), https://doi.org/10.1002/pssr.201700107.
[55] C. Lu, Rusli, A.B. Prakoso, H. Wang, Hole selective WOx and V2Ox contacts using solution process for silicon solar cells application, Mater. Chem. Phys. 273 (2021), https://doi.org/10.1016/j.matchemphys.2021.125101.
[56] L.G. Gerling, et al., Transition metal oxides as hole-selective contacts in silicon heterojunctions solar cells, Sol. Energy Mater. Sol. Cell. 145 (2016) 109–115, https://doi.org/10.1016/j.solmat.2015.08.028.
[57] G. Masmitjà, et al., V2O: X-based hole-selective contacts for c-Si interdigitated back-contacted solar cells, J Mater Chem A Mater 5 (19) (2017) 9182–9189, https://doi.org/10.1039/c7ta01959a.
[58] C. Liu, et al., Tuning oxygen vacancies in vanadium-doped molybdenum oxide for silicon solar cells with hole selective contact, Mater. Sci. Semicond. Process. 146 (2022), https://doi.org/10.1016/j.mssp.2022.106687.
[59] M. Mews, L. Korte, B. Rech, Oxygen vacancies in tungsten oxide and their influence on tungsten oxide/silicon heterojunction solar cells, Sol. Energy Mater. Sol. Cell. 158 (2016) 77–83, https://doi.org/10.1016/j.solmat.2016.05.042.
[60] H.J. Zhai, B. Kiran, L.F. Cui, X. Li, D.A. Dixon, L.S. Wang, Electronic structure and chemical bonding in Mon- and Mon clusters (M = Mo, W; n = 3-5): a photoelectron spectroscopy and ab initio study, J. Am. Chem. Soc. 126 (49) (2004) 16134–16141, https://doi.org/10.1021/ja046536s.
[61] S.F. Vyboishchikov, J. Sauer, Gas-phase vanadium oxide anions: structure and detachment energies from density functional calculations, J. Phys. Chem. A 104 (46) (2000) 10913–10922, https://doi.org/10.1021/jp001936x.
[62] J. Kumari, J.S. Bhardwaj, Rahul, P. Agarwal, Oxygen plasma treatment of thermally evaporated MoO $_{3-x}$ films: an approach to tune the work function, ACS Appl. Electron. Mater. (2023), https://doi.org/10.1021/acsaelm.3c00343.
[63] D. Wrana, K. Cieślik, W. Belza, C. Rodenbücher, K. Szot, F. Krok, Kelvin probe force microscopy work function characterization of transition metal oxide crystals under ongoing reduction and oxidation, Beilstein J. Nanotechnol. 10 (2019) 1596–1607, https://doi.org/10.3762/bjnano.10.155.
[64] S. Chen, J.R. Manders, S.W. Tsang, F. So, Metal oxides for interface engineering in polymer solar cells, J. Mater. Chem. 22 (46) (2012) 24202–24212, https://doi.org/10.1039/c2jm33838f.
[65] Ü. Akin, H. Şafak, Thickness dependence of dispersion parameters of the MoOx thin films prepared using the vacuum evaporation technique, J. Alloys Compd. 647 (2015) 146–151, https://doi.org/10.1016/j.jallcom.2015.06.164.
[66] L. Giordano, G. Pacchioni, Oxide films at the nanoscale: new structures, new functions, and new materials, Acc. Chem. Res. 44 (11) (2011) 1244–1252, https://doi.org/10.1021/ar200139y.
[67] Y. Guo, J. Robertson, Origin of the high work function and high conductivity of MoO3, Appl. Phys. Lett. 105 (22) (2014), https://doi.org/10.1063/1.4903538.
[68] Y. Zhao, Hydrogenated nanocrystalline silicon-based layers for silicon heterojunction and perovskite/c-Si tandem solar cells. https://doi.org/10.4233/uuid:d848c617-2eae-491d-aae1-d524495e9e65, 2023.
[69] E. Horynová, et al., Optical characterization of low temperature amorphous MoOx, WOX, and VOx prepared by pulsed laser deposition, Thin Solid Films 693 (Jan) (2020), https://doi.org/10.1016/j.tsf.2019.137690.